Physicochemical Characterisation of a Na-H-F Thermal Battery Material

Terry D. Humphries,*[†] Aditya Rawal,[‡] Matthew R. Rowles, [†∫] Christopher R. Prause,[†] Julianne E. Bird,[†] Mark Paskevicius,[†] M. Veronica Sofianos,[†] Craig. E. Buckley[†]

[†] Physics and Astronomy, Fuels and Energy Technology Institute, Curtin University, GPO Box U1987, Perth, WA 6845, Australia.

[‡] Nuclear Magnetic Resonance Facility, Mark Wainwright Analytical Centre, The University of New South Wales, Sydney, NSW 2052, Australia.

[∫] John De Laeter Centre, Curtin University, GPO Box U1987, Perth, WA 6845, Australia.

ABSTRACT: Fluorine-substituted sodium hydride is investigated for application as a thermal energy storage material inside thermal batteries. A range of compositions of NaH_xF_{1-x} (x = 0, 0.5, 0.7, 0.85, 0.95, 1) have been studied using synchrotron radiation powder X-ray diffraction (SR-XRD), near edge X-ray absorption fine structure spectroscopy (NEXAFS), and nuclear magnetic resonance spectroscopy (NMR), with the thermal conductivity and melting points also being determined. SR-XRD and NMR spectroscopy studies identified that the solid solutions formed during synthesis contain multiple phases rather than a single stoichiometric compound, despite the materials exhibiting a single melting point. As the fluorine content of the materials increases, the Na−H(F) bond length decreases, increasing the stability of the compound. This trend is also observed during the melting point analysis where increasing the fluorine content increases the melting point of the material, i.e. $x < 0.3$ (i.e. $F^- > 0.7$) enables melting at temperatures above 750 °C.

1. INTRODUCTION

The future of global energy supply and demand is consistently on the political and economic agenda. At the same time, governments are realising that hydrogen must be in the frame due to its high energy density, and relative ease of production and storage compared to alternative energy storage media.[1] Currently, high-density storage is one of the key challenges to overcome for the hydrogen economy, although metal hydrides are able to reversibly store hydrogen at an ever decreasing cost. The reaction of metal with hydrogen is an exothermic reaction and much research has been conducted to use metal hydrides as thermal energy stores, also known as thermal batteries.[2-6] Metal hydrides are materials that have potential for multiple technological applications, including as a fuel for vehicles and infrastructure, thermal and electrical batteries, and smart windows.[4, 6-14] These applications require drastically diverse physical properties from the hydride, although the prevailing characteristic is that hydrogen must be stored reversibly to be cost effective.

Thermal batteries can be designed to store waste heat produced during industrial processes (e.g. smelting plants or refineries) or from concentrating solar power, where the stored heat can be released upon demand to produce electricity.[4, 6, 15-16] To optimise thermal-to-electrical conversion efficiency, the thermal batteries should have high operating temperatures of > 600 °C, although low-temperature applications, such as centralised heating/cooling, solar cooking, or greenhouse heating have also been identified.[15-16] Three methods of thermal energy storage have been identified: (i) sensible, (ii) latent, and (iii) thermochemical heat storage. A full review of these methods has been previously undertaken,[17-18] identifying thermochemical heat storage as the most energy dense. During thermochemical heat storage the heat is stored by way of an endothermic process of breaking chemical bonds between elements (e.g Na−H), whilst heat is released during the exothermic process of forming bonds. An example of this process is the reversible hydrogenation of metals, of which a host of metal hydrides have been reported to be potential materials for high-temperature thermal batteries, including NaH, MgH_2, $NaMgH_3$, $FeTiH_x$, CaH_2, CaH_2/2Al and Mg_2FeH_6. Lab-scale prototypes have also been developed to illustrate the potential of thermal batteries.[2-6, 11-12, 19-25]

An inherent problem with employing Na or Mg as the base metal in a thermal battery is their low vapour pressure, which causes the metal to segregate during cycling at elevated operating temperatures.[19, 24] A recent method to inhibit metal segregation, and to also increase the operating temperatures and/or reduce the hydrogen operating pressure, is to stoichiometrically substitute F^- for H^-. A variety of these systems have been explored and physically characterised including $NaMgH_2F$,[26] NaH_xF_{1-x}, and $Mg(H_xF_{1-x})_2$ (x = 0.5, 0.7, 0.85, 0.95, 1).[19, 24] In these systems, segregation is inhibited by the formation of the metal fluoride during hydrogen release (e.g. $NaMgF_3$, NaF or MgF_2, respectively). Some segregation is reported to occur at higher temperatures, although further investigations have shown that encapsulation of the powder in iron tubes is beneficial.[19]

Despite the evaporative problems associated with NaH_xF_{1-x} upon dehydrogenation, the physical properties displayed by this material still make it attractive as a thermal battery mate-

rial. Pure NaH has an enthalpy ΔH_{des} = 117 kJ/mol H_2 and entropy ΔS_{des} = 167 J/K/mol H_2 change during hydrogen release, and as such has an operating temperature range of 427 – 660 °C (1 – 150 bar H_2).[21, 27] Due to the additional stability provided by F^- substitution, $NaH_{0.5}F_{0.5}$ has modified thermodynamics ΔH_{des} = 106 kJ/mol H_2 and ΔS_{des} = 143 J/K/mol H_2, and as such has an operating temperature range of 468 – 773 °C (1 – 150 bar H_2).[19] It is noted that ΔH_{des} actually decreases with increasing F content, which is counterintuitive when considering the material undergoes stabilisation, but the significant decrease in ΔS_{des} provides the main contribution to the material's thermal stabilisation due to the reduction of molecular rearrangement required.

In addition to applying NaH complexes as a thermal battery based on thermochemical heat storage, NaH has the potential to be applied as a latent heat or phase-change material (PCM) for thermal batteries. NaH has a melting point of 632 °C, but in order to avoid hydrogen desorption (a reaction that could be used for thermochemical heat storage), a significant hydrogen back pressure is required.[21, 28] For instance, NaH decomposes to Na at 427 °C under 1 bar H_2,[27] while NaH requires a pressure of > 106 bar H_2 to prevent decomposition when it melts at 632 °C with an associated heat of fusion ΔH_{fus} = 26.6 kJ/mol or 1108 kJ/kg.[28] Although this energy is less than the thermochemical storage capacity of NaH of 2434 kJ/kg, there are advantages to employing NaH as a PCM. For instance, a chemical reaction is not taking place, and as such, hydrogen will not need to be stored in a separate low-pressure store during hydrogen desorption, resulting in a reduction in engineering and materials costs. In addition, the ΔH_{fus} = 1108 kJ/kg is higher than many other compounds including LiF (1041 kJ/kg) and LiF-MgF_2 (947 kJ/kg).[29]

NaH_xF_{1-x} may prove to be a PCM that could operate at increased temperatures and require lower H_2 back-pressure compared to NaH. It is expected that increasing the F content will make the melting point tend towards the melting point of NaF (995 °C),[30] whilst a lower back-pressure would be required due to the increased thermodynamic stabilisation of the F-rich materials. For instance, $NaH_{0.5}F_{0.5}$ would only require approximately 22.5 bar H_2 to prevent decomposition at 632 °C, compared to 115 bar for pure NaH based on its thermodynamics.[19, 28]

Previous studies have reported the physical characterisation of NaH and NaF by various techniques including X-ray and neutron powder diffraction (XRD; NPD);[19, 31-32] and vibrational,[33-34] nuclear magnetic resonance (NMR)[35-36] and X-ray fluorescence (XRF) spectroscopies.[37-41] These studies have underlined the differences between these isomorphous materials, but very little is known of their solid-solutions apart from their crystallographic and thermodynamic properties. In this study, the NaH_xF_{1-x} (x = 0, 0.5, 0.7, 0.85, 0.95, 1) system has been investigated by X-ray diffraction, ^{1}H and ^{23}Na NMR spectroscopy and near-edge X-ray absorption fine structure spectroscopy (NEXAFS, see ESI for details) to investigate the bonding differences between the solid-state solution systems. In addition, the melting point of these materials has been determined to assess their application as a PCM for thermal battery technologies, while their thermal conductivities have also been established.

2. EXPERIMENTAL SECTON

2.1. Synthesis and manipulation. All manipulation of chemicals was undertaken in an argon-atmosphere Mbraun Unilab glovebox in order to minimise oxygen (O_2 < 1 ppm) and water (H_2O < 1 ppm) contamination. NaH (95%, Sigma-Aldrich) and NaF (99.99%, Sigma-Aldrich) were ball milled at various stoichiometric ratios (Table 1) inside an Across International Planetary Ball Mill (PQ-N04) employing tempered 316 stainless steel vials and balls in an Ar atmosphere. A ball-to-powder mass ratio of 30:1 was employed, with a total milling time of 3 h at a speed of 400 rpm. This method of synthesis has been shown to be ideal for this class of material.[19, 42] Following milling, the samples were generally annealed under a H_2 pressure of 40 bar at 460 °C for 6 days to form solid solutions.

2.2. Powder X-ray diffraction. Synchrotron radiation powder X-ray diffraction (SR-XRD) was performed on the PD beamline at the Australian Synchrotron in Melbourne, Australia.[43] NaH_xF_{1-x} powder was loaded in a quartz capillary (outer diameter 0.7 mm, wall thickness 0.01 mm) and mounted in a sample holder with Swagelok tube fittings inside a glove box filled with purified argon (< 1 ppm O_2 and H_2O). The sample holder was then connected to a H_2 gas filling/vacuum manifold and placed under 1 bar H_2 atmosphere. The NaF sample was measured in a sealed quartz capillary. One-dimensional SR-XRD patterns (monochromatic X-rays with λ = 0.824890(1) Å) were collected at room temperature using a Mythen microstrip detector[44] with an exposure time of 54 s. The capillary was oscillated 120° to improve the powder averaging. Diffraction patterns were quantitatively analysed with the Rietveld method[45] using TOPAS (Bruker-AXS).[46] The low atomic number of hydrogen usually presents difficulties for Rietveld refinement of hydrogen containing phases from X-ray data. However, the occupancy of hydrogen and fluorine can be readily obtained for NaH_xF_{1-x} solid solutions due to dramatic changes in diffracted peak intensities that occur upon fluorine substitution for hydrogen.

Laboratory powder X-ray diffraction was conducted on a Bruker D8 advance (Cu-$K_{\alpha 1+2}$ radiation, λ = 1.5418 Å) equipped with a LynxEye 3° linear position sensitive detector (PSD). A 2θ acquisition range was typically between 20° and 80°. To prevent sample oxidation occurring during data acquisition, samples were loaded into an air-tight spherically capped poly-methylmethacrylate (PMMA) sample holder. The sample holder caused a broad hump in the diffraction profile in the region where 2θ equals 20°.

2.3. NMR Spectroscopy. Solid-state ^{1}H, and ^{23}Na Magic Angle Spinning (MAS) Nuclear Magnetic Resonance (NMR) experiments were carried out on a narrow-bore Bruker Biospin Avance III solids-700 MHz spectrometer with a 16.4 Tesla superconducting magnet operating at frequencies of 700 MHz, and 185 MHz for the ^{1}H, and ^{23}Na nuclei respectively. Approximately 3 - 10 mg of material was packed into 2.5 mm zirconia rotors fitted with Vespel® caps and spun to 28 kHz at the magic angle. The one dimensional ^{1}H and ^{23}Na spectra were acquired with hard 2.5 µs and 2 µs radio frequency pulses corresponding to 90° and 30° tip angles respectively. The recycle delays of up to 1000 s and 10 s for the ^{1}H and ^{23}Na nuclei were used to ensure full relaxation of the signals. 32 and 1024 transients were co-added for the ^{1}H and ^{23}Na experiments to ensure sufficient signal to noise. The ^{1}H NMR shifts were referenced to solid adamantane at 1.8 ppm whilst the ^{23}Na NMR shifts were referenced to the signal of solid NaCl

(δ_{cs} = 0 ppm) obtained at 28 kHz MAS, to account for sample heating during the fast MAS (Note: For 0.1 M aqueous NaCl, δ = -7.2 ppm against solid NaCl).[35] The ^{23}Na 2D MQMAS (multiple-quantum magic-angle spinning) spectra were acquired with a triple-quantum pulse sequence with an excitation pulse of 8.5 μs, a conversion pulse of 2.5 μs with a 20 μs z-filter followed by a 60 μs selective 90° pulse for detection. The spectral deconvolution was carried out using the Dmfit software.[47]

2.4. Melting Point Analysis. Melting point analysis was carried out inside a custom built high pressure (150 bar) autoclave reactor composed of Haynes 230 Inconel alloy. A K-type thermocouple was inserted through the top of the reactor so that it sat 1 cm from the bottom of the vessel before ~4 g of sample was loaded to ensure adequate penetration into the sample. The heating profile was set with an initial ramp of 20 °C/min to maximum temperature followed by two cycles with heating and cooling at 2 °C/min. The range of cycling temperatures varied between samples with a maximum range of 560 – 770 °C. During cycling, temperature was recorded every 2 seconds. To prevent the pressure from exceeding the reactor rating, the initial pressure was set at 140 bar and vented gradually maintain 140 bar until the maximum cycling temperature was reached. Endo/exothermic phase transition temperatures were determined by identifying sharp discontinuities in the temperature derivative with respect to time.

2.5 Thermal Conductivity, Thermal Diffusivity and Specific heat The thermal conductivity (λ_{TC}), thermal diffusivity (k) and and the heat capacity per unit volume (C) was measured using the TPS 500S (Hot Disk, Thermtest). The TPS 500S uses a double nickel spiral sensor (2 mm radius), laminated by electrically insulating Kapton. Measurements were undertaken in an argon atmosphere at a constant ambient temperature. 1.5 g of NaH_xF_{1-x} (x = 0, 0.5, 0.70, 0.85, 1) was pressed in a 13 mm diameter die with a manual hydraulic press (370 MPa for 5 minutes). The sensor was firmly clamped co-centrically between the pellets. In these experiments, the isotropic module was utilised, calculating the geometric mean value of the radial thermal conductivity in the probed sample volume. Fine-tuned analysis occurred with the first 20 to 200 data points, generating the transient and residual graphs. 10 measurements per sample were conducted, with 15 minutes in between each measurement to allow the sample and sensor to cool.

3. RESULTS AND DISCUSSION

3.1. Powder X-ray diffraction. NaH and NaF both exist in the cubic space group $Fm\bar{3}m$, and have crystallographic lattice parameters (*LP*) of 4.8812(2) and 4.63397(1) Å, respectively after annealing (Table 1, Figure 1(a)). This difference is a consequence of the decreased ionic radius of F^- (1.33 Å) compared to H^- (1.4 - 2.1 Å),[48] and increased electronegativity of F^- (F^- = 3.98, H^- = 2.20)[49] which ensures a reduction in bond distance with Na–H = 2.44061(8) Å and Na–F = 2.316985(5) Å (Table 1, Figure 1(b)).[31-32] Upon formation of Na−H−F solid-solutions, a near linear correlation between H/F composition and lattice parameters has been previously observed, although bond distances have not been discussed.[19] Na and H(F) occupy the crystallographic special sites 4*a* and 4*b*, respectively, and so bond lengths can be deduced directly from the lattice parameter. Due to the cubic atomic arrangement, the Na−H and Na−F distances would be expected to be averaged to avoid disorder and perhaps altering the atomic symmetry. A direct correlation is observed between an increase in Na−H(F) bond distance with increasing H^- content (Table 1, Figure 1(b)). This is best described as a polynomial increase with a R^2 factor of 0.9992 (Figure 1(a)). It must be noted that the Na−H distance of 2.44061(8) Å is within 2% error of the 2.445 Å determined by neutron powder diffraction at room temperature,[32] hence the values reported here are validated.

The non-linearity of the *LP* and Na−H(F) bond length as a function of H^- content is likely attributed to the steric hindrance caused by the H^- as x approaches 1 in NaH_xF_{1-x}. It is known that the ionic size of H^- can vary between 1.4 − 2.1 Å[48], and it has been calculated to be 1.40 Å in LiH.[50] Although the ionic radius expansion of the unit cell as F^- occupancy diminishes. In NaF, the F−F bond distance is 3.276662(5) Å, which increases of H^- is similar to the size of F^- (1.33 Å), the 9% increase in size may become significant enough to invoke a greater to 3.3826(2) Å in $NaH_{0.7}F_{0.3}$ and 3.45154(8) Å in NaH (Table 1). As the crystal system is cubic, all of the bond distances and lattice parameters increase by 5.3 % from NaF to NaH.

Each of the NaH_xF_{1-x} samples were analysed to determine the homogeneity of the solid solutions (Table S1, ESI). This analysis was undertaken by quantitative Rietveld refinement of the SR-XRD data with an input of eleven NaH_xF_{1-x} phases

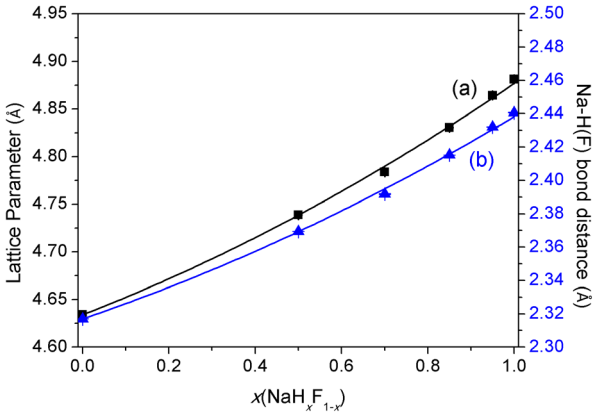

Figure 1. (a) Lattice parameter and (b) Na−H(F) bond distance for NaH_xF_{1-x} (x = 0, 0.5, 0.7, 0.85, 0.95, 1) solid solutions determined by SR-XRD. Lattice parameter: $y = 0.089x^2 = 0.1564x + 4.6345$. Na−H(F) bond distance: $y = 0.0446x^2 + 0.0781x + 2.3173$.

Table 1. Lattice parameter (*LP*), Na−H(F), and H(F)−H(F) bond distances for each NaH_xF_{1-x} (x = 0, 0.5, 0.7, 0.85, 0.95, 1) solid-solution determined by SR-XRD at room temperature. Estimated standard deviations (ESDs) are in parentheses.

x(NaH_xF_{1-x})	*LP* (Å)	Na−H(F) (Å)	H(F)−H(F) (Å)
0	4.63397(1)	2.316985(5)	3.276662(5)
0.50	4.73884(3)	2.36942(2)	3.35086(2)
0.70	4.7837(4)	2.3918(2)	3.3826(2)
0.85	4.83049(5)	2.41525(3)	3.41568(3)
0.95	4.8642(1)	2.43208(6)	3.43948(6)
1	4.8812(2)	2.44061(8)	3.45154(8)

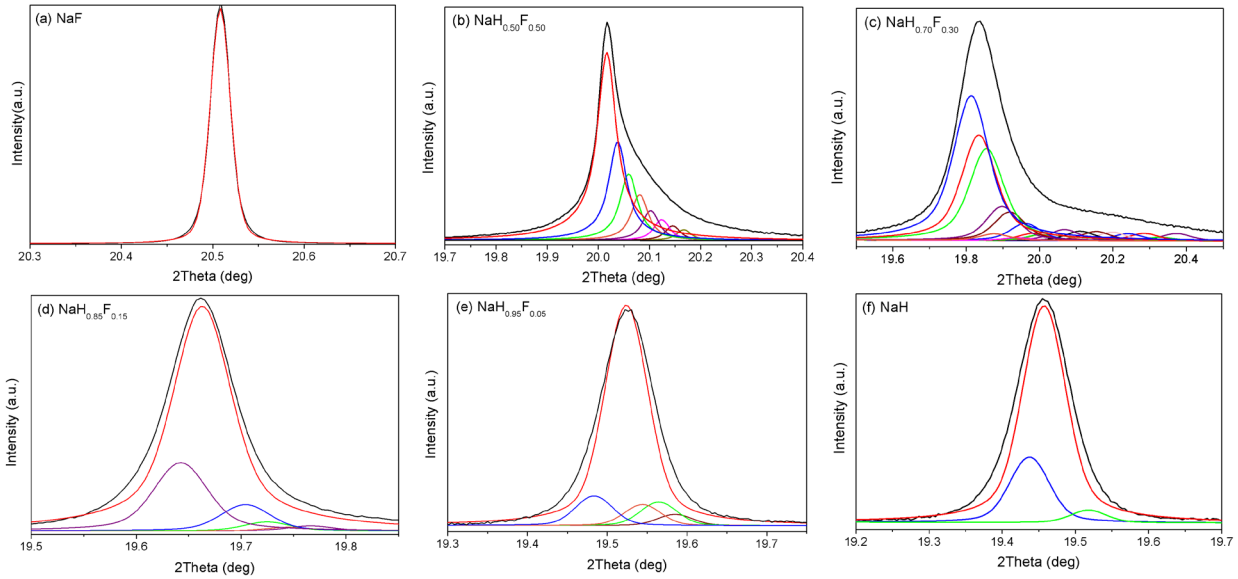

Figure 2. Phase distribution in NaH_xF_{1-x} solid solutions determined by SR-XRD as observed at the (002) Bragg peak (space group $Fm\bar{3}m$). Black curves indicate the data measured by XRD, remaining curves indicate the modelled phases. λ = 0.824890(1) Å, T = 27 °C.

(21 for $NaH_{0.70}F_{0.30}$) allowing the *LP* and H/F occupancy to refine freely. Due to the limit of quantification, only phases with greater than 1.0 wt% have been used for quantitative analaysis. Table S1 details the *LP* and quantification of any determined Na−H−F phases, while Figure 2 illustrates that data while focusing on the (002) Bragg peak. For a homogeneous sample, a single symmetric peak would be observed, however phase segregation is apparently inherent for all samples, but increases with F^- concentration. This is observed as asymmetry of the peaks. For NaH_xF_{1-x} samples with x = 0.70 and 0.50, there were at least 7 phases identified, with each phase containing a slightly different lattice parameter and therefore a slightly different H:F ratio. $NaH_{0.7}F_{0.3}$ had the largest spread, with the second largest phase quantified to 26.4 wt%. Using a quadratic function to correlate the *LP* with x in in NaH_xF_{1-x} it was determined that x for the $NaH_{0.7}F_{0.3}$ sample ranged from 0.70 (30.2 wt%) to 0.57 (2.1 wt%).

3.2. NMR Spectroscopy. The solid-state NMR spectra illustrate that, as with the SR-XRD results, there are multiple chemical environments observed in the NaH_xF_{1-x} mixtures (Figure 3). Analysis of pure NaH by ^{23}Na NMR yields a single signal symmetric peak centred at 11 ppm, consistent with the highly symmetric environment and consequently low quadrupolar coupling for the ^{23}Na nucleus. Upon addition of stoichiometric quantities of F^-, an increasing number of smaller peaks are observed, mainly shifted to lower ppm. The ^{23}Na NMR signals, which are best resolved for $NaH_{0.50}F_{0.50}$, clearly indicate the formation of distinct phases with different H:F ratios as indicated by the XRD measurements. Careful analysis of the ^{23}Na signals however shows that initially, the primary peak is shifted to slightly higher ppm with F^- addition: 11.5, 12.1 and 12.5 ppm (for x = 0.95, 0.85 and 0.70 respectively). Pure NaF has been reported to have a chemical shift of ~ 8ppm.[51] The distribution of peaks, especially with increasing F^- content, is indicative of species with altered Na environments, which is due to the different distributions of F^- and H^- in the first coordination sphere around the Na^+.[52] This

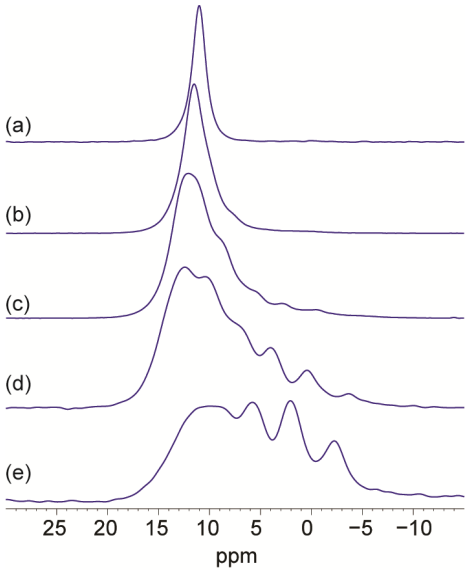

Figure 3. ^{23}Na MAS NMR spectra of NaH_xF_{1-x} for (a) x = 1, (b) x = 0.95, (c) x = 0.85, (d) x = 0.70 and (e) x = 0.50.

therefore corroborates the observations in the SR-XRD data, in that single phases are not being obtained.

Broadening of the primary peak is evident for $NaH_{0.50}F_{0.50}$, where the primary peak maximum is at 9.5 ppm. The increased peak broadening (of the primary peak) likely indicates a two-fold effect of increased quadrupolar coupling brought about by a degree of asymmetry in the local bonding around the ^{23}Na nucleus as well as an increase in the disorder of the primary phase due to the milling process. In comparison, the multiple new peaks that are formed have a narrower line width, indicating that they originate from ordered crystalline environments, which are forming with the increased addition of NaF. Compared to the ^{23}Na NMR, the ^{1}H NMR is not informative, with the ^{1}H spectra for the different compositions yielding a similar signal (Figure S1, ESI).

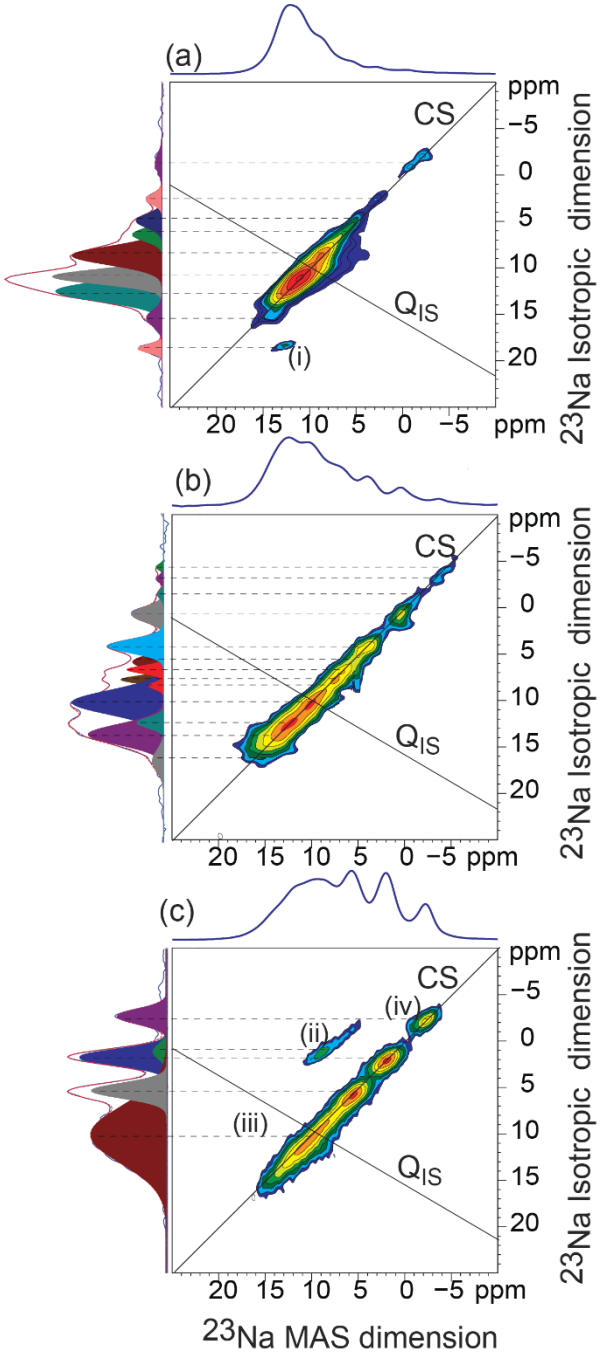

Figure 4. ^{23}Na MQMAS NMR of (a) $NaH_{0.85}F_{0.15}$, (b) $NaH_{0.70}F_{0.30}$ and (c) $NaH_{0.50}F_{0.50}$. The MAS spectra are plotted on the top, while the isotropic projections are plotted to the left. The CS axis with slope 1 describes the chemical shift distributions, while the Q_{IS} axis describes the variation in the quadrupolar shifts. The gaussian fits to the isotropic projections are presented as filled peaks.

Considering the wide NMR shift distribution observed for the ^{23}Na, the formulations x = 0.85, 0.70 and 0.50 were further investigated via 2D MQMAS spectroscopy (Figure 4). The complexity of resolving signal with a disorder induced chemical shift dispersion as well as quadrupolar interaction can be addressed via the MQMAS experiment, which separates the isotropic and quadrupolar interactions along two distinct axes.[53] Thus the 2D MQMAS experiment can separate signals that would otherwise overlap in the 1D NMR. A fit to the isotropic signals from the MQMAS experiment reveals that there are 9, 13 and 5 resolvable ^{23}Na sites for x = 0.85, 0.70 and 0.50 respectively. The high number of sites observed for x = 0.70 agrees with the XRD refinements. Sites marked (i) and (ii) for x = 0.85 and x = 0.50 (Figure 4 (a) and (c) respectively) lie off the main chemical shift (CS - defined as the trace of the chemical shift tensor in its principal axis frame) axis indicating that they have a more distinct quadrupolar shift than the NaH/F phase and are therefore attributed to impurities, such as NaOH, in the material. While the peaks are broadened to a degree along the CS axis, for example, site (iii) in Figure 4 (c), there is relatively little dispersion along the Q_{IS} axis, which does increase with increasing values of x. This indicates that at low NaF substitution, ($NaH_{0.85}F_{0.15}$), there is greater disorder, likely caused by the incorporation of the F^- into the NaH lattice, which induces a degree of disorder. At greater F^- content, it may be thermodynamically favourable for multiple crystalline phase segregation to occur, which is evidenced by the reduced dispersion along the Q_{IS} axis. Within this context, it is likely that the broadening for the isotropic peak (iii) observed for $NaH_{0.50}F_{0.50}$, is not a result of disorder, since it would be expected to also result in a concomitant dispersion of the quadrupolar shift, which is seen for example in disordered pervoskites.[54-55] Instead it is likely a result of multiple ^{23}Na sites within the NaH/F family that are not sufficiently chemically resolved, and therefore have a large spectral overlap. Finally, we note that the peak marked (iv) for x = 0.5, having the lowest chemical shift is likely some unreacted "pure" NaF phase.

3.3. Melting Point Analysis. The solid-liquid phase transition temperatures for NaH_xF_{1-x} (x = 1, 0.85, 0.50) were measured through temperature measurements during thermal ramps whilst maintaining a hydrogen pressure of 150 bar to minimise the possibility of sample decomposition. According to thermodynamic analysis, NaH is stable up to 659 °C under 150 bar H_2 pressure, whilst the most stable compound of the series studied here should be $NaH_{0.50}F_{0.50}$, which should decompose at 775 °C under 150 bar H_2.[19, 27] Therefore, although the other compounds in this series have not had their thermodynamics experimentally determined, their temperature of desorption will fall between 659 and 775 °C under 150 bar H_2 backpressure (Table 2). For pure NaH, a sharp thermal signal was observed (Figure S2(a), ESI) and a phase transition temperature of 625.2 ± 6.5 °C was extrapolated. This is in agreement with the accepted value of 632 °C.[28]

For $NaH_{0.85}F_{0.15}$, the melting point was not as defined as for NaH although an inflection in the temperature data is visible at 662.5 ± 7.7 °C (Figure S2(b), ESI). The possibility of phase segregation was investigated by XRD analysis of the temperature cycled material. Visual inspection of the $NaH_{0.85}F_{0.15}$ cycled product shows two distinctive phases, one white and one grey-white, while powder XRD confirmed the occurrence of phase segregation (Figure S3, ESI). Analysis of the data for the cycled material suggests at least three NaH_xF_{1-x} phases exist, along with some Na and NaOH. The XRD of the cycled $NaH_{0.85}F_{0.15}$ (Figure S3(b), ESI) is considerably altered compared to the synthesised material. The synthesised material has Bragg peaks at 2θ = 28, 48 and 56° which are only seen in hydrogen rich samples.[19] Post cycling, these peaks have disappeared completely, while the remaining peaks have shifted to higher angles indicating the sample has become more fluorine rich. A small peak at 2θ = 29.5° also indicates the presence of metallic sodium and hence

Table 2. Thermal Transport Properties of NaH_xF_{1-x} (x = 1, 0.85, 0.7, 0.5, 0) samples, where λ_{TC} is thermal conductivity (W/m.K), k is thermal diffusivity (mm²/s), and C is the heat capacity per unit volume (MJ/m³.K). Crystallite size determined from the SR-XRD data using TOPAS.[46]

Sample	λ_{TC} (W/m.K)	k (mm²/s)	C (MJ/m³.K)	Crystallite size (nm)	Melting point (°C)
NaF	9.4(1)	1.8(2)	5.5(6)	256	995[a]
$NaH_{0.5}F_{0.5}$	0.870(2)	0.73(1)	1.20(2)	4489	> 750
$NaH_{0.85}F_{0.15}$	1.490(6)	0.72(3)	2.00(8)	206	662.5(77)
NaH	4.98(7)	1.1(1)	4.7(4)	4490	625.2(65)

[a] Ref [30]

decomposition has occurred to an extent. While 140 bar H_2 should be enough to prevent a uniform sample of $NaH_{0.85}F_{0.15}$ from decomposing at these temperatures, if the NaH phase segregates decomposition will occur.[19]

At the maximum temperature of the cycle of 720 °C, NaH requires a hydrogen back pressure of 430 bar. As such, under the experiment conditions employed here, decomposition will occur.Upon heating $NaH_{0.50}F_{0.50}$ to 750 °C, no apparent change in the temperature gradient was observed indicating that no phase change or decomposition event occurred (Figs. S2(c), ESI). The addition of fluorine to NaH causes a large increase in phase transition temperature, due to increased thermal efficiencies at higher temperatures. NaF has previously been determined to melt at 995 °C,[30] therefore $NaH_{0.50}F_{0.50}$ and $NaH_{0.70}F_{0.30}$ are expected to melt before this point. However, without instrumentation that can hold greater than 150 bar H_2 at temperatures above 750 °C it is not possible to determine their melting point. It is assumed that phase segregation will occur as $NaH_{0.50}F_{0.50}$ has been shown to segregate during hydrogen cycling at 520 °C.[19]

3.4. Thermal Conductivity, Thermal Diffusivity and Heat Capacity. The average thermal transport properties of NaH_xF_{1-x} (x = 1, 0.85, 0.70, 0.50, 0) are presented in Table 2. A non-linear relationship between these thermal transport properties and amount of H/F present was evident (Figure 5). The data collected for NaF correlates well with data available in databases (λ_{TC} = 10.5 W/m·K, k = 3.7 mm²/s, C = 2.8 MJ/m³·K).[56] Thermal transport properties are highly dependent on sample preparation and measurement conditions, and these conditions are often not defined clearly in the existing literature e.g. refs [56-57]. Each sample in the present study was measured under identical conditions with identically prepared pellets being measured under an Ar atmosphere. Each of the determined properties (λ_{TC}, k and C) show that the fluorine substituted materials exhibited less favourable thermal properties than their pure counterparts. This effect does not appear to be directly related to the crystallite size, as shown in Table 2.

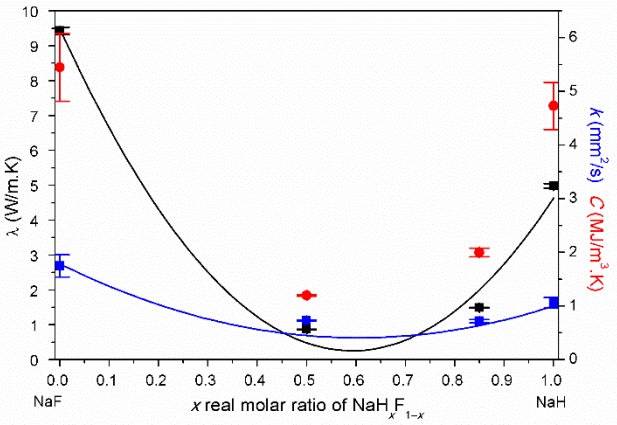

Figure 5. Relationship between thermal transport properties (■ Thermal Conductivity, ■ Thermal Diffusivity and ● Heat Capacity per unit volume) and composition in NaH_xF_{1-x}.

4. CONCLUSIONS

This study has detailed a thorough characterisation of fluorine substituted sodium hydride (NaH_xF_{1-x} where x = 1, 0.95, 0.85, 0.70, 0.50, 0), a class of materials that have potential application as thermal energy storage materials. The physical properties of these solid solutions have been probed by XRD, NMR, NEXAFS, phase transition analysis and thermal conductivity. A contraction of the cubic crystal lattice is observed upon addition of F^- into the unit cell, which is largely due to the smaller ionic radius of the F^- compared to H^-. This ultimately leads to a reduction in Na-H(F) bond distance. SR-XRD and NMR spectroscopy determined that a single phase NaH_xF_{1-x} solid solution is not formed upon annealing for 6 days at 450 °C but rather a mixture of stoichiometries with an average H:F ratio close to expected.

The melting point analysis of these materials allowed a feasibility study for application as phase change materials for thermal energy storage. The initial melting points increase with F^- content although upon cycling, phase segregation occurs.

The thermal transport properties, including thermal conductivity, diffusivity and heat capacity, for the range of NaH_xF_{1-x} samples were also determined. This was the first time that NaH and NaF have been measured under the same conditions as each other, which has allowed a direct comparison with the fluorine substituted analogues. Thermal conductivity and diffusivity is seen to decrease for the substituted samples and is likely due to the random distribution of F^- within the lattice.

To ensure technological application, a homogeneous solid solution may be required. Overall, this may reduce the risk of phase segregation. The utilisation of common laboratory powder X-ray diffractometry may not allow identification of inhomogeneity with solid solutions as the Bragg peaks measured are often broad and may hide slight asymmetry. This study has shown that MAS-NMR is suitable to determine whether multiple phases are present. Annealing for longer than six days may increase the homogeneity of the sample but if technologi-

cal application is to be achieved then sample preparation time may be key. NaF is also a hard material and so reduction of particle size before ball milling may also increase homogeneity.

ASSOCIATED CONTENT

Supporting Information.
Quantitative Rietveld analysis of SR-XRD data for NaH_xF_{1-x} solid solutions; ^1H NMR spectra of NaH_xF_{1-x}; Melting point analysis data; NEXAFS data.
This material is available free of charge via the Internet at http://pubs.acs.org."

AUTHOR INFORMATION

Corresponding Author

* E-mail: terry_humphries81@hotmail.com

Author Contributions

All authors have given approval to the final version of the manuscript.

Notes

The authors declare no competing financial interest.

ACKNOWLEDGMENT

The authors CEB, TDH, MVS and MP acknowledge the financial support of the Australian Research Council (ARC) for ARC Linkage grants LP120101848 and LP150100730. CEB, TDH, MP and MVS acknowledge financial support from the Department of Industry Innovation and Science for the 2019 Global Innovation Linkage (GIL73589) grant. MP acknowledges his ARC Future Fellowship FT160100303. Powder Diffraction and NEXAFS measurements were undertaken at the Australian Synchrotron, part of ANSTO. The authors are grateful for the technical support of B. Cowie and A. Tadich of the Australian Synchrotron. The authors would also like to acknowledge Dr J.P. Veder for collecting the NEXAFS data.

REFERENCES

1. Bruce, S.; Temminghoff, M.; Hayward, J.; Schmidt, E.; Munnings, C.; Palfreyman, D.; Hartley, P., National Hydrogen Roadmap. CSIRO, Australia: 2018.
2. Dong, D.; Humphries, T. D.; Sheppard, D. A.; Stansby, B.; Paskevicius, M.; Sofianos, M. V.; Chaudhary, A. L.; Dornheim, M.; Buckley, C. E., Thermal Optimisation of Metal Hydride Reactors for Thermal Energy Storage Applications. *Sustain. Energy Fuels* **2017,** *1* (8), 1820-1829.
3. Felderhoff, M.; Urbanczyk, R.; Peil, S., Thermochemical Heat Storage for High Temperature Applications – A Review. *Green* **2013,** *3* (2), 113-123.
4. Manickam, K.; Mistry, P.; Walker, G.; Grant, D.; Buckley, C. E.; Humphries, T. D.; Paskevicius, M.; Jensen, T.; Albert, R.; Peinecke, K., et al., Future Perspectives of Thermal Energy Storage with Metal Hydrides. *Int. J. Hydrogen Energy* **2019,** *44* (15), 7738-7745.
5. Paskevicius, M.; Sheppard, D. A.; Williamson, K.; Buckley, C. E., Metal Hydride Thermal Heat Storage Prototype for Concentrating Solar Thermal Power. *Energy* **2015,** *88*, 469-477.
6. Sheppard, D. A.; Paskevicius, M.; Humphries, T. D.; Felderhoff, M.; Capurso, G.; von Colbe, J. B.; Dornheim, M.; Klassen, T.; Ward, P. A.; Teprovich, J. A., et al., Metal Hydrides for Concentrating Solar Thermal Power Energy Storage. *Appl. Phys. A* **2016,** *122* (4), 395.
7. Humphries, T. D.; Sheppard, D. A.; Buckley, C. E., Recent Advances in the 18-electron Complex Transition Metal Hydrides of Ni, Fe, Co and Ru. *Coord. Chem. Rev.* **2017,** *342*, 19-33.
8. Lai, Q.; Paskevicius, M.; Sheppard, D. A.; Buckley, C. E.; Thornton, A. W.; Hill, M. R.; Gu, Q.; Mao, J.; Huang, Z.; Liu, H. K., et al., Hydrogen Storage Materials for Mobile and Stationary Applications: Current State of the Art. *ChemSusChem* **2015,** *8* (17), 2789-825.
9. Møller, K. T.; Sheppard, D. A.; Ravnsbæk, D.; Buckley, C. E.; Akiba, E.; Li, H.-W.; Jensen, T. R., Complex Metal Hydrides for Hydrogen, Thermal and Electrochemical Energy Storage. *Energies* **2017,** *10* (10), 1645.
10. Frommen, C.; Sorby, M. H.; Heere, M.; Humphries, T. D.; Olsen, J. E.; Hauback, B. C., Rare Earth Borohydrides-Crystal Structures and Thermal Properties. *Energies* **2017,** *10* (12), 2115.
11. Poupin, L.; Humphries, T. D.; Paskevicius, M.; Buckley, C. E., A Thermal Energy Storage Prototype Using Sodium Magnesium Hydride. *Sustain. Energy Fuels* **2019,** *3* (4), 985-995.
12. Poupin, L.; Humphries, T. D.; Paskevicius, M.; Buckley, C. E., An Experimental High Temperature Thermal Battery Coupled to a Low Temperature Metal Hydride for Solar Thermal Energy Storage. *Sustain. Energy Fuels* **2020,** *4* (1), 285-292.
13. Yartys, V. A.; Lototskyy, M. V.; Akiba, E.; Albert, R.; Antonov, V. E.; Ares, J. R.; Baricco, M.; Bourgeois, N.; Buckley, C. E.; Bellosta von Colbe, J. M., et al., Magnesium Based Materials for Hydrogen Based Energy Storage: Past, Present and Future. *Int. J. Hydrogen Energy* **2019,** *44* (15), 7809-7859.
14. Hirscher, M.; Yartys, V. A.; Baricco, M.; Bellosta von Colbe, J.; Blanchard, D.; Bowman, R. C.; Broom, D. P.; Buckley, C. E.; Chang, F.; Chen, P., et al., Materials for hydrogen-based energy storage – Past, recent progress and future outlook. *J. Alloys Compd.* **2019**, 153548.
15. Sharma, S. D.; Kitano, H.; Sagara, K., Phase Change Materials for Low Temperature Solar Thermal Applications. *Res. Rep. Fac. Eng. Mie Univ* **2004,** *29* (1), 31-64.
16. Pereira da Cunha, J.; Eames, P., Thermal Energy Storage for Low and Medium Temperature Applications Using Phase Change Materials – A Review. *Appl. Energy* **2016,** *177*, 227-238.
17. Liu, D.; Xin-Feng, L.; Bo, L.; Si-quan, Z.; Yan, X., Progress in Thermochemical Energy Storage for Concentrated Solar Power: A review. *Int. J. Energy Res.* **2018,** *42* (15), 4546-4561.
18. Prieto, C.; Cooper, P.; Fernandez, A. I.; Cabeza, L. F., Review of Technology: Thermochemical Energy Storage for Concentrated Solar Power Plants. *Renewable & Sustainable Energy Reviews* **2016,** *60*, 909-929.
19. Humphries, T. D.; Sheppard, D. A.; Rowles, M. R.; Sofianos, M. V.; Buckley, C. E., Fluoride Substitution in Sodium Hydride for Thermal Energy Storage Applications. *J. Mater. Chem. A* **2016,** *4* (31), 12170-12178.
20. Sheppard, D. A.; Humphries, T. D.; Buckley, C. E., What is Old is New Again. *Mater. Today* **2015,** *18* (8), 414-415.
21. Sheppard, D. A.; Humphries, T. D.; Buckley, C. E., Sodium-Based Hydrides for Thermal Energy Applications. *Appl. Phys. A* **2016,** *122* (4), 406.
22. Sheppard, D. A.; Paskevicius, M.; Buckley, C. E., Thermodynamics of hydrogen desorption from $NaMgH_3$ and its application as a solar heat storage medium. *Chem. Mater.* **2011,** *23* (19), 4298-4300.
23. Urbanczyk, R.; Meggouh, M.; Moury, R.; Peinecke, K.; Peil, S.; Felderhoff, M., Demonstration of Mg_2FeH_6 as Heat Storage Material at Temperatures up to 550 Degrees C. *Appl. Phys. A* **2016,** *122* (4), 315.
24. Tortoza, M. S.; Humphries, T. D.; Sheppard, D. A.; Paskevicius, M.; Rowles, M. R.; Sofianos, M. V.; Aguey-Zinsou, K. F.; Buckley, C. E., Thermodynamics and Performance of the Mg-H-F System for Thermochemical Energy Storage Applications. *Phys. Chem. Chem. Phys.* **2018,** *20* (4), 2274-2283.
25. Ward, P. A.; Teprovich, J. A.; Liu, Y. F.; He, J.; Zidan, R., High Temperature Thermal Energy Storage in the $CaAl_2$ System. *J. Alloys Compd.* **2018,** *735*, 2611-2615.

26. Sheppard, D. A.; Corgnale, C.; Hardy, B.; Motyka, T.; Zidan, R.; Paskevicius, M.; Buckley, C. E., Hydriding Characteristics of $NaMgH_2F$ with Preliminary Technical and Cost Evaluation of Magnesium-Based Metal Hydride Materials for Concentrating Solar Power Thermal Storage. *RSC Adv.* **2014,** *4* (51), 26552-26562.

27. Manchester, F. D.; San-Martin, A., *Phase Diagrams of Binary Hydrogen Alloys*. ASM International: Ohio, 2000.

28. Klostermeier, W.; Franck, E. U., Liquid-Mixtures of Sodium and Sodium Hydride at High-Pressures and Temperatures. *Berichte Der Bunsen-Gesellschaft-Physical Chemistry Chemical Physics* **1982,** *86* (7), 606-612.

29. Kenisarin, M. M., High-Temperature Phase Change Materials for Thermal Energy Storage. *Renew. Sustain. Energy Rev.* **2010,** *14* (3), 955-970.

30. Cantor, S., Freezing Point Depressions in Sodium Fluoride. Effect of Alkaline Earth Fluorides. *J. Phys. Chem.* **1961,** *65* (12), 2208-2210.

31. Shirako, Y.; Shi, Y. G.; Aimi, A.; Mori, D.; Kojitani, H.; Yamaura, K.; Inaguma, Y.; Akaogi, M., High-Pressure Stability Relations, Crystal Structures, and Physical Properties of Perovskite and Post-Perovskite of $NaNiF_3$. *J. Solid State Chem.* **2012,** *191*, 167-174.

32. Shull, C. G.; Wollan, E. O.; Morton, G. A.; Davidson, W. L., Neutron Diffraction Studies of NaH and NaD. *Phys. Rev.* **1948,** *73* (8), 842-847.

33. Maki, A. G.; Olson, W. B., Infrared-Spectrum of Sodium Hydride. *J. Chem. Phys.* **1989,** *90* (12), 6887-6892.

34. Huang, H. Y.; Lu, T. L.; Whang, T. J.; Chang, Y. Y.; Tsai, C. C., Dissociation Energy of the Ground State of NaH. *J. Chem. Phys.* **2010,** *133* (4), 044301.

35. Koller, H.; Engelhardt, G.; Kentgens, A. P. M.; Sauer, J., ^{23}Na NMR Spectroscopy of Solids: Interpretation of Quadrupole Interaction Parameters and Chemical Shifts. *J. Phys. Chem.* **1994,** *98* (6), 1544-1551.

36. Reeve, Z. E.; Franko, C. J.; Harris, K. J.; Yadegari, H.; Sun, X.; Goward, G. R., Detection of Electrochemical Reaction Products from the Sodium-Oxygen Cell with Solid-State ^{23}Na NMR Spectroscopy. *J. Am. Chem. Soc.* **2017,** *139* (2), 595-598.

37. Hudson, E.; Moler, E.; Zheng, Y.; Kellar, S.; Heimann, P.; Hussain, Z.; Shirley, D. A., Near-Edge Dodium and Fluorine K-Shell Photoabsorption of Alkali Halides. *Phys Rev B Condens Matter* **1994,** *49* (6), 3701-3708.

38. Natoli, C. R., *EXAFS and Near Edge Structure*. Springer: NewYork, 1983.

39. Neuville, D. R.; Cormier, L.; Flank, A. M.; Prado, R. J.; Lagarde, P., Na K-Edge XANES Spectra of Minerals and Glasses. *Eur. J. Mineral.* **2004,** *16* (5), 809-816.

40. Teodorescu, C. M.; El Afif, A.; Esteva, J. M.; Karnatak, R. C., Na 1s Excitations in Vapor and Solid Sodium Halides. *Phys. Rev. B* **2001,** *63* (23), 233106.

41. Prado, R. J.; Flank, A. M., Sodium K-Edge XANES Calculation in 'NaCl' Type Structures. *Phys. Scr.* **2005,** *T115*, 165-167.

42. Huot, J.; Cuevas, F.; Deledda, S.; Edalati, K.; Filinchuk, Y.; Grosdidier, T.; Hauback, B. C.; Heere, M.; Jensen, T. R.; Latroche, M., et al., Mechanochemistry of Metal Hydrides: Recent Advances. *Materials (Basel)* **2019,** *12* (17), 2778.

43. Wallwork, K. S.; Kennedy, B. J.; Wang, D., The High Resolution Powder Diffraction Beamline for the Australian Synchrotron. *Synchrotron Radiation Instrumentation, Pts 1 and 2* **2007,** *879* (1), 879-+.

44. Schmitt, B.; Bronnimann, C.; Eikenberry, E. F.; Gozzo, F.; Hormann, C.; Horisberger, R.; Patterson, B., Mythen Detector System. *Nucl Instrum Meth A* **2003,** *501* (1), 267-272.

45. Young, R. A.; Young, R. A., *The Rietveld Method*. Oxford University Press: 1995.

46. Coelho, A. A., TOPAS and TOPAS-Academic: An Optimization Program Integrating Computer Algebra and Crystallographic Objects Written in C Plus. *J. Appl. Crystallogr.* **2018,** *51* (1), 210-218.

47. Massiot, D.; Fayon, F.; Capron, M.; King, I.; Le Calve, S.; Alonso, B.; Durand, J. O.; Bujoli, B.; Gan, Z. H.; Hoatson, G., Modelling One- and Two-Dimensional Solid-State NMR Spectra. *Magn. Reson. Chem.* **2002,** *40* (1), 70-76.

48. Takagi, S.; Orimo, S., Recent Progress in Hydrogen-Rich Materials from the Perspective of Bonding Flexibility of Hydrogen. *Scr. Mater.* **2015,** *109*, 1-5.

49. Pauling, L., The Nature of the Chemical Bond. Iv. The Energy of Single Bonds and the Relative Electronegativity of Atoms. *J. Am. Chem. Soc.* **1932,** *54* (9), 3570-3582.

50. Lang, P. F.; Smith, B. C., Ionic Radii for Group 1 and Group 2 Halide, Hydride, Fluoride, Oxide, Sulfide, Selenide and Telluride Crystals. *Dalton Trans.* **2010,** *39* (33), 7786-91.

51. Rude, L. H.; Filso, U.; D'Anna, V.; Spyratou, A.; Richter, B.; Hino, S.; Zavorotynska, O.; Baricco, M.; Sorby, M. H.; Hauback, B. C., et al., Hydrogen-Fluorine Exchange in $NaBH_4$-$NaBF_4$. *Phys. Chem. Chem. Phys.* **2013,** *15* (41), 18185-18194.

52. Jensen, S. R. H.; Jepsen, L. H.; Skibsted, J.; Jensen, T. R., Phase Diagram for the $NaBH_4$-KBH_4 System and the Stability of a $Na_{1-x}K_xBH_4$ Solid Solution. *J. Phys. Chem. C* **2015,** *119* (50), 27919-27929.

53. Frydman, L.; Harwood, J. S., Isotropic Spectra of Half-Integer Quadrupolar Spins from Bidimensional Magic-Angle-Spinning Nmr. *J. Am. Chem. Soc.* **1995,** *117* (19), 5367-5368.

54. Ghasemian, M. B.; Rawal, A.; Liu, Y.; Wang, D., Approaching Piezoelectric Response of Pb-Piezoelectrics in Hydrothermally Synthesized Bi0.5(Na1- xK x)0.5TiO3 Nanotubes. *ACS Appl. Mater. Interfaces* **2018,** *10* (24), 20816-20825.

55. Ghasemian, M. B.; Rawal, A.; Wang, F.; Chu, D.; Wang, D., Lattice Evolution and Enhanced Piezoelectric Properties of Hydrothermally Synthesised $0.94(Bi_{0.5}Na_{0.5})TiO_3$–$0.06BaTiO_3$ Nanofibers. *J. Mater. Chem. C* **2017,** *5* (42), 10976-10984.

56. Thermtest Thermal Properties Materials Database. https://thermtest.com/materials-database (accessed October 27, 2019).

57. Haynes, W. M., *CRC Handbook of Chemistry and Physics, 96th Edition (Internet Version 2016)*. CRC Press/Taylor and Franci: Boca Raton, FL, 2016.

TOC Graphic

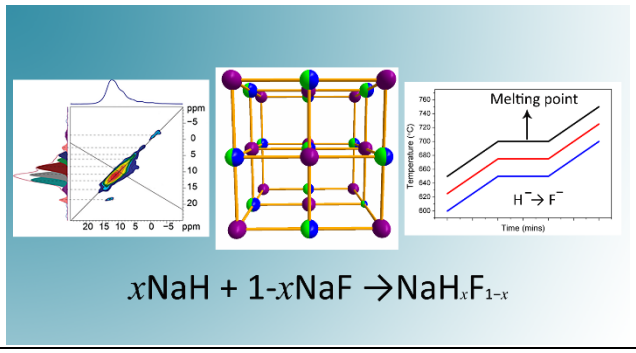
ppm
−5
0
5
10
15
20
20 15 10 5 0 −5 ppm
Melting point
Temperature (°C)
760
740
720
700
680
660
640
620
600
H⁻→ F⁻
Time (mins)
xNaH + 1-xNaF →NaHxF1−x